Small-displacement mechanical energy harvesting through magnetic phase transition materials

Zhengming Zhang,[1,7] Tongtong Zhou,[1,7] Yong Hu,[2] Hongchang Wang,[1] Chenyu Zhang,[2] Xucai Kan,[3] Kun Xu,[4] Bo Yang,[2] Yongle Li,[1] Pengyu Zhao,[5] Zuhua Chen,[6] Pengtao Cheng,[1] Hanghang Fu,[1] Zhe Li,[4] Chengliang Zhang,[1,*] and Dunhui Wang[1,5,*]

*Correspondence: clzhang@hdu.edu.cn(C. Z.); wangdh@hdu.edu.cn(D.W.)

Received: January 16, 2025; Accepted: April 22, 2025; https://doi.org/10.59717/j.xinn-energy.2025.100098

GRAPHICAL ABSTRACT

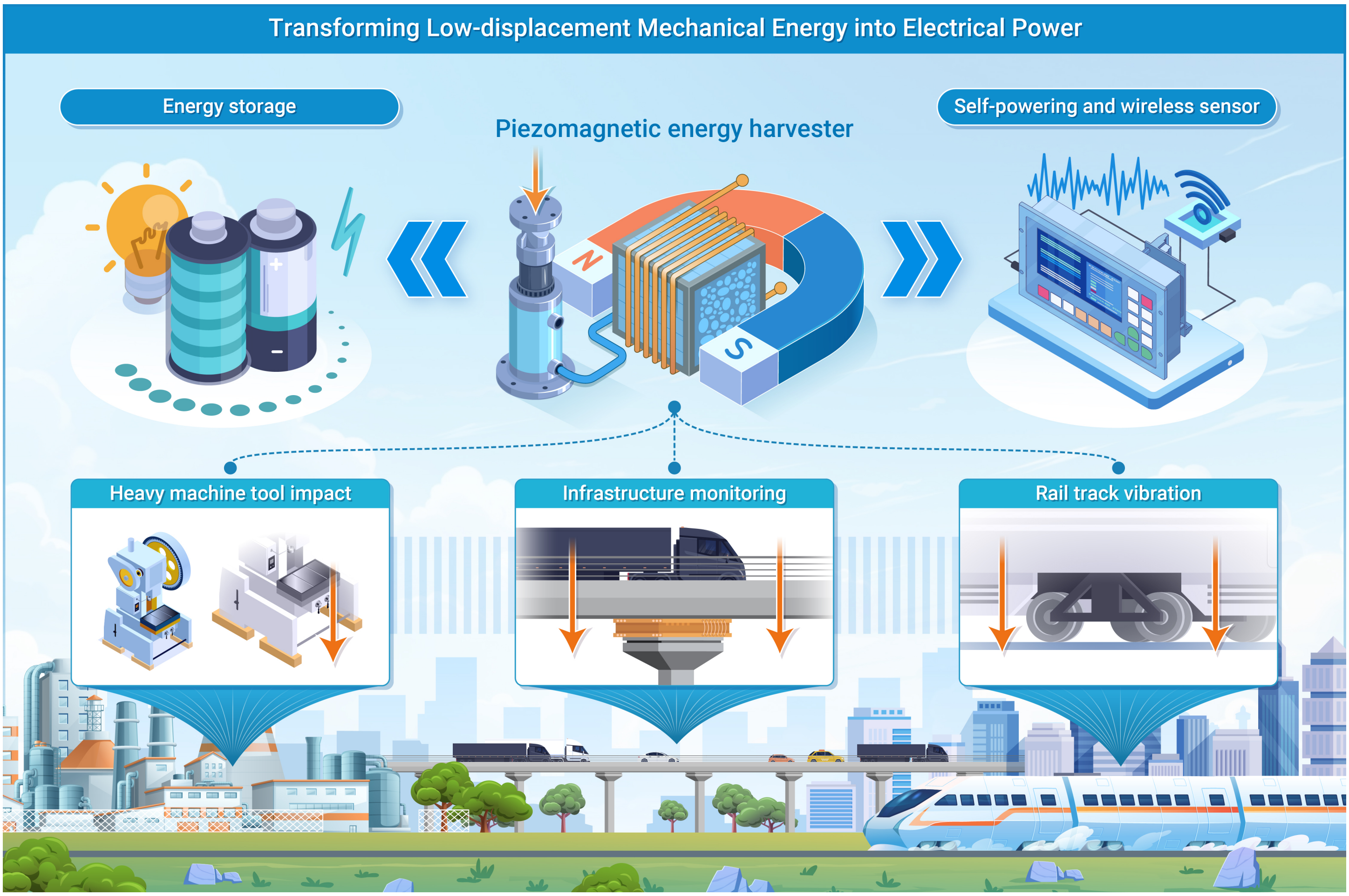

PUBLIC SUMMARY

- Innovative low-displacement mechanical energy harvesting using piezomagnetic effects.
- $MnCoSi_{0.88}Ge_{0.12}$ exhibits excellent piezomagnetic properties over a broad temperature range.
- Prototype device achieves 34.4 μW/cm^3 power density with no moving parts.
- Effective energy harvesting from small-displacement vibrations and impacts.
- Potential for self-powered sensor networks in harsh, unattended environments.

REPORT

Small-displacement mechanical energy harvesting through magnetic phase transition materials

Zhengming Zhang,[1,7] Tongtong Zhou,[1,7] Yong Hu,[2] Hongchang Wang,[1] Chenyu Zhang,[2] Xucai Kan,[3] Kun Xu,[4] Bo Yang,[2] Yongle Li,[1] Pengyu Zhao,[5] Zuhua Chen,[6] Pengtao Cheng,[1] Hanghang Fu,[1] Zhe Li,[4] Chengliang Zhang,[1,*] and Dunhui Wang[1,5,*]

[1]Hangzhou Dianzi University, Hangzhou, 310018, China

[2]College of Sciences and Key Laboratory for Anisotropy and Texture of Materials (Ministry of Education), Northeastern University, Shenyang 110819, 110819, China

[3]Engineering Technology Research Center of Magnetic Materials, Anhui University, Hefei 230601, China

[4]School of Physics and Electronic Engineering, Qujing Normal University, Qujing 655011, China

[5]National Laboratory of Solid State Microstructures, Nanjing University, Nanjing 210093, China

[6]Technical Institute of Physics and Chemistry, Chinese Academy of Sciences, Beijing 100190, China

[7]These authors contributed equally to this work.

*Correspondence: clzhang@hdu.edu.cn(C. Z.); wangdh@hdu.edu.cn(D.W.)

Received: January 16, 2025; Accepted: April 22, 2025; https://doi.org/10.59717/j.xinn-energy.2025.100098

Citation: Zhang Z., Zhou T., Hu Y., et al. (2025). Small-displacement mechanical energy harvesting through magnetic phase transition materials. *The Innovation Energy* **2**:100098.

Our daily environment contains abundant vibrational and impact energies characterized by high instantaneous stress yet minimal displacement. These inherent characteristics present fundamental conversion challenges for traditional generators, which require substantial relative motion between magnetic and conductive components to induce effective current generation. To address this limitation, we propose an innovative method of low-displacement mechanical energy harvesting that utilizes piezomagnetic effects during pressure-induced magnetic phase transitions. By doping germanium into the silicon site of MnCoSi, the magnetic phase transition material $MnCoSi_{0.88}Ge_{0.12}$ exhibits excellent piezomagnetic properties over a broad temperature range. Our meticulously designed piezomagnetic power prototype device features a magnetic circuit that enhances magnetic flux within the induction coil. Using $MnCoSi_{0.88}Ge_{0.12}$ as the working substance, the prototype is rigorously tested under various temperatures and pressures, exhibiting intriguing performance from 250 to 325 K, covering room temperature. Notably, the prototype device, which is devoid of moving parts, has achieved a peak power density of 34.4 μW/cm³. The device's ability to harvest energy from small-displacement vibrations and instantaneous impacts, such as those from heavy machinery or geological activities, highlights its potential for applications in mobile energy supply. This work also provides a path toward self-powered vibration and impact sensor networks in harsh and unattended environments.

INTRODUCTION

In the face of growing energy demands and accelerating climate commitments, the development of sustainable energy conversion technologies has reached critical urgency.[1-3] To address this dual challenge, converting dormant energy into usable electricity emerges as a strategic priority for optimizing energy systems. Notably, established technologies such as wind turbines and thermoelectric generators have demonstrated success in harvesting macroscopic energy flows, particularly in industrial waste heat recovery scenarios[4,5]. However, a significant technological gap persists in harvesting ubiquitous mechanical energy sources—from industrial machinery vibrations to traffic oscillations —primarily due to their high instantaneous stress and minimal displacement characteristics.

Conventional generators require substantial displacement between magnets and inductive coils, making them incompatible with these small-displacement vibrations and impacts. Although piezoelectric ceramics offer an alternative transduction pathway, their widespread adoption is hindered by intrinsic material constraints including depolarization under cyclic loading and limited lifespans due to their inherent brittleness.[6-9] Additionally, the magnetostrictive effect and Villari effect can also be used for harvesting magnetic[10-13] and mechanical energy.[14] However, conventional magnetostrictive materials (e.g., Terfenol-D, Galfenol) contain expensive metals and exhibit performance that depends critically on specific crystal orientations and magnetic/stress fields alignment,[15,16] limiting practical deployment. Collectively, these challenges demand new transduction mechanisms to reliably convert minimal mechanical displacements into stable electrical outputs.

Phase transition materials uniquely exhibit substantial changes in disorder in response to temperature, magnetic fields, or stress.[17] Although current research mainly focuses on energy-efficient and environmentally friendly applications such as magnetocaloric,[18,19] barocaloric,[20-22] elastocaloric cooling,[23,24] and heat storge,[25] there is an emerging interest in harnessing magnetic phase transitions for energy conversion, such as transforming waste heat into electrical energy.[26-32] Nonetheless, studies on the transformation of mechanical energy into electrical energy through magnetic phase transition mechanisms remain scarce. Magnetic phase transition materials commonly exhibit an inherent coupling between exchange interaction and atomic spacing, manifesting as mutual couplings between magnetism and the lattice structure. The application of a magnetic field to induce a phase transition often leads to exchange competition, subsequently altering the magnetic atomic spacing and resulting in pronounced magnetostriction behavior.[33-35] Conversely, the application of pressure can induce variations in the spacing between magnetic atoms, affecting the exchange interaction and potentially generating new magnetic ordered structures. This, in turn, alters the overall magnetization of the material, producing the phenomenon known as the piezomagnetic effect. Notable examples include the pressure-induced antiferromagnetic to ferrimagnetic transition and the large piezomagnetic effect observed in antiperovskite $Mn_3Ga_{0.95}N_{0.94}$,[36] and the giant piezomagnetic effect in Fe-doped $Mn_{0.87}Fe_{0.13}NiGe$ due to pressure-driven spin reorientation.[37] It is particularly noteworthy that the application of small-displacement impact forces to magnetic phase-transition solids enables rapid magnetization changes while preventing structural collapse. This phenomenon arises from the material's capacity for effective strain propagation,[38,39] combined with the fundamental property of exceptionally low volumetric compressibility in solids,[20] which inherently resists bulk compression under external forces. By integrating Faraday's law of electromagnetic induction with the piezomagnetic effect, it is anticipated that magnetic phase transition materials could achieve efficient conversion of small-displacement mechanical energy into electrical energy.

It is recognized that magnetic phase transition materials, widely used in refrigeration technologies, struggle with narrow operational temperature ranges that also hinder their use in piezomagnetic power generation. This constraint drives the demand for developing materials with broad-temperature piezomagnetic effects, particularly spanning room temperature. The MnCoSi alloy stands out in this pursuit. Its unique helical antiferromagnetic structure allows magnetic field-induced transitions to a ferromagnetic state across a wide temperature span below the Néel temperature of 381 K.[33,40,41] Importantly, the phase transition in MnCoSi is accompanied by orthorhombic lattice distortions,[42] which is likely to bring about a wide temperature range of piezomagnetic effects due to strong magnetoelastic coupling. Notably, the strategic substitution of a modest amount of Ge for Si in the alloy can effectively reduce the critical magnetic field of the MnCoSi alloy.[34,43] This modification also shifts the transition point to a cooler temperature range, enabling reversible second-order phase transitions to be achieved at room temperature.[34,43]

In this report, we have confirmed that the magnetic phase transition mate-

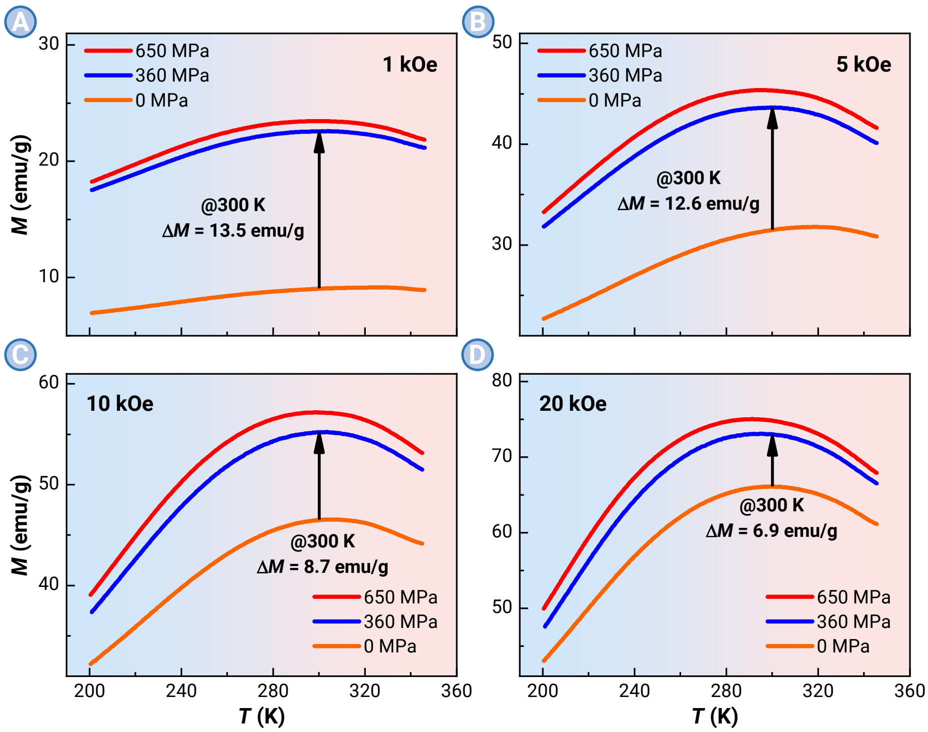

Figure 1. *M-T* curves under pressures of 0, 360, and 650 MPa for the $MnCoSi_{0.88}Ge_{0.12}$ alloy measured at different magnetic fields. (A) H = 1 kOe. (B) H = 5 kOe. (C) H = 10 kOe. (D) H = 20 kOe.

rial $MnCoSi_{0.88}Ge_{0.12}$ maintains stable piezomagnetic properties across a broad temperature range, including room temperature. Unlike conventional generators, piezomagnetic power generation through magnetic phase transition functions reliably without the necessity of moving components. Based on this mechanism, we design a novel magnetic circuit structure and construct a functional prototype. Under cyclic loading (5 Hz, 0-100 MPa), the device achieves a maximum power density of 34.4 μW/cm³. Additionally, the piezomagnetic effect in the $MnCoSi_{0.88}Ge_{0.12}$ alloys is driven by hydrostatic pressure transmitted via a paraffin wax medium, rather than by axial stress. This eliminates concerns about sample mechanical strength and orientation. These results validate piezomagnetic power generation as a viable energy conversion strategy, particularly suitable for portable power systems and vibration-driven sensor networks.

MATERIALS AND METHODS

Sample growth and measurements

The $MnCoSi_{0.88}Ge_{0.12}$ polycrystalline alloy samples were fabricated via arc melting in an argon atmosphere of high purity, employing high-purity elemental materials. To attain a uniform composition across the alloy, the melting process was meticulously repeated 3 to 4 times for each sample. The ingots were crushed and transferred into quartz glass tubes for subsequent processing. To counteract the substantial negative thermal expansion associated with the structural phase transformation that the alloy undergoes during furnace cooling, a dual-layer containment approach was adopted. The initial quartz tubes were nested within a larger quartz tube and subjected to high vacuum sealing to mitigate the risk of tube shattering. The vacuum-sealed, double-layer quartz tubes containing the alloy samples were positioned in a high-temperature annealing furnace. The samples were heated to a temperature of 1500 K, which is proximal to the alloy's melting point of approximately 1473 K, and maintained at this temperature for 30 minutes to facilitate complete annealing.

Magnetization measurements were performed using a vibrating sample magnetometer (VSM, Versalab, Quantum Design Inc.) with a copper-beryllium clamp-type high-pressure cell, designed to handle pressures up to 1.30 GPa. Daphne oil was employed as the medium for transmitting pressure within the system. Sample pressures were determined by the compression length of the copper-beryllium cell. We recorded temperature-dependent magnetization (M–T) curves at magnetic fields of 1, 5, 10, and 20 kOe, and isothermal magnetization curves from 260 to 320 K at 20 K intervals, all under pressures of 0, 360, and 650 MPa.

Numerical simulations

Finite element simulation was carried out using the COMSOL Multiphysics software (Version 5.5). The AC/DC module was employed to model the response of magnetic flux density (B) distribution in the parallel branches to variations in the magnetic permeability (μ) of the piezomagnetic sample. The simulated result was compared with the experimental data to validate the accuracy of the model. Additionally, the impact of air gap spacing on the magnetic flux density distribution was investigated through finite element analysis, as detailed in Supplementary Note 2.

Piezomagnetic power generation prototype device

The magnetomotive force was provided by permanent magnets in the piezomagnetic power generation prototype device. The variation of Φ_m with alternating external pressure was detected by an induction coil, which in turn output an induced electromotive force. Alternating pressure of different frequencies and intensities was applied to the prototype using a pressure testing machine (YEW-50, Jinan Tianchen, China). The induction coil of the prototype had 3880 turns, and its output end was connected to a digital multimeter (TH1963, Tonghui, China) to achieve real-time recording of the V. To study the effect of temperature on the piezomagnetic effect of the $MnCoSi_{0.88}Ge_{0.12}$ alloy, a temperature control apparatus was designed and constructed (See Supplementary Note 4 for details).

RESULTS AND DISCUSSION

Piezomagnetic properties of $MnCoSi_{0.88}Ge_{0.12}$

Figure 1 displays the temperature-dependent magnetization (M–T) curves for the $MnCoSi_{0.88}Ge_{0.12}$ alloy under pressures of 0, 360, and 650 MPa measured at 1, 5, 10, and 20 kOe. It is observed that the magnetization of the $MnCoSi_{0.88}Ge_{0.12}$ alloy is consistently enhanced by the applied pressure within the temperature range of 200 K to 345 K, demonstrating its remarkable piezomagnetic properties across a broad temperature range. Specifically, at a magnetic field of 1 kOe and a temperature of 300 K, the increase in magnetization (ΔM) of the alloy is observed to be 13.5 emu/g as the pressure gradually increases from 0 MPa to 360 MPa. Further increasing the pressure to 650 MPa produces a comparable magnetization enhancement of 14.4 emu/g. Moreover, the peak positions of the M-T curves tend to shift towards lower temperatures at applied pressure due to the pressure-assisted antiferromagnetic to ferromagnetic phase transition, which has also been observed in MnCoSi alloys.[41]

The pressure-induced enhancement of ferromagnetism is further supported by the isothermal magnetization (M-H) curves at various temperatures, as illustrated in Figure 2. At 280 K and 300 K, a maximum ΔM of 15.8 emu/g and 15.9 emu/g is observed respectively, with pressure increasing from 0 to 360 MPa at 2 kOe. Similarly, at 260 K and 320 K, the maximum ΔM values are 15.7 emu/g and 15.3 emu/g under the same conditions. It is widely believed that in MnCoSi-based materials, a smaller volume correlates with a higher magnetic state, while a larger volume is associated with a lower magnetic state.[42] When pressure is applied, the volume of the crystal cell decreases, which in turn favors the high magnetic state.[42,44] Moreover, the MnCoSi system experiences anisotropic lattice distortions under pressure, with the a-axis contracting and the b- and c-axes expanding.[41] Along the c-

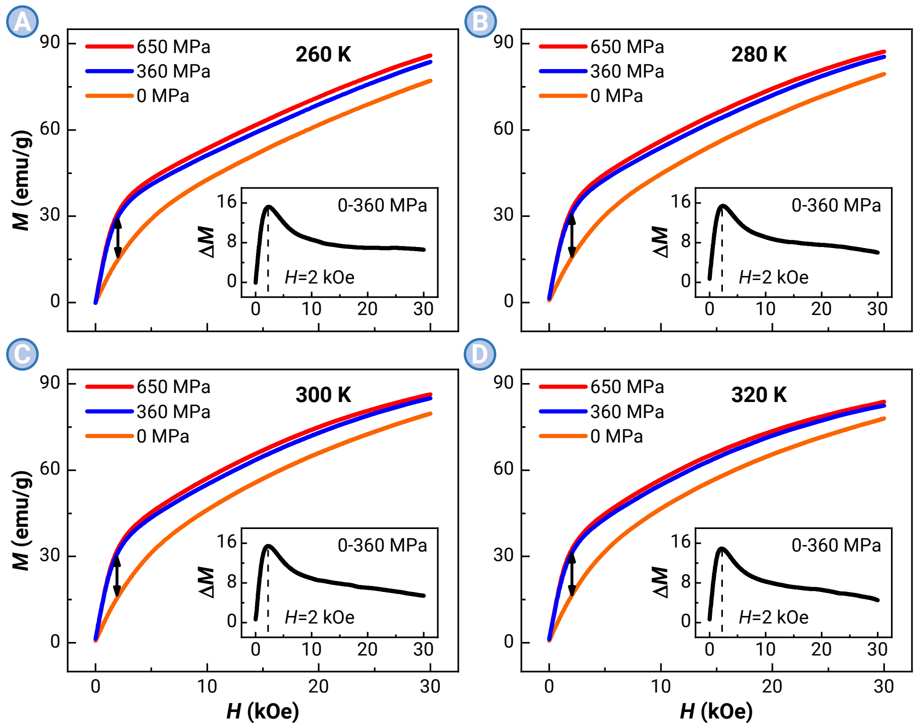

Figure 2. *M-H* curves under pressures of 0, 360, and 650 MPa for the $MnCoSi_{0.88}Ge_{0.12}$ alloy measured at different temperatures. (A) 260 K. (B) 280 K. (C) 300 K. (D) 320 K.

axis direction, the interatomic distance between Mn atoms (d_1) increases with the application of pressure, leading to a transition from an antiferromagnetic ground state to a ferromagnetic configuration.[33] These results confirm the $MnCoSi_{0.88}Ge_{0.12}$ alloy's piezomagnetic properties across a broad temperature range including room temperature, which is crucial for practical applications.

Design of a piezomagnetic power generation prototype device

We have engineered a piezomagnetic power generation device. Central to this device is a pressure-sensitive magnetic reluctance unit, which comprises a pressure chamber filled with piezomagnetic sample, as depicted in Figure 3A. The chamber's side walls are constructed from magnetically conductive and non-magnetic materials, with two cylindrical walls serving as magnetic poles, providing a magnetic field perpendicular to the cylinder's axis for the sample within the tube. The press rod and base are crafted from non-magnetic materials. The magnetic permeability (μ) of the piezomagnetic material varies with pressure, rendering it equivalent to a pressure-sensitive magnetic reluctance, expressed as $R_m = \frac{L}{\mu A}$, where R_m is the magnetic reluctance along the magnetization direction, L is the material's length in this direction, and A is its cross-sectional area.

To translate variations in magnetic reluctance into detectable changes in magnetic flux (Φ_m) and generate an induced electromotive force in the induction coil, we have positioned the pressure-sensitive magnetic reluctance and the induction coil in parallel branches. Two series-connected permanent magnets supply the magnetic flux potential for these branches. Employing the finite element simulation tool COMSOL Multiphysics, we have analyzed how the Φ_m distribution in the parallel branches responds to changes in the piezomagnetic sample's μ, as shown in Figure 3B. At low μ values (e.g., μ=1), the magnetic reluctance of the pressure-sensitive branch is higher, directing most of the Φ_m through the induction coil branch. Conversely, at high μ values (e.g., μ=100), the magnetic reluctance of the pressure-sensitive branch decreases, reallocating a portion of Φ_m to this branch. The device's performance is directly related to the Φ_m distribution between the two branches. To optimize this distribution, an adjustable air gap is introduced into the induction coil branch, as depicted in Figure 3C. This enables fine-tuning of the induction coil's magnetic reluctance, balances the magnetic flux density (B) in both branches, and maximizes the change in magnetic flux density (ΔB) within the induction coil.

In setting the air gap width, it is crucial to ensure that all parts of the magnetic core operate within the linear region of the magnetization curve. This prevents waveform distortion of the induction voltage and manages magnetic leakage loss. Based on the *M-H* curves of the $MnCoSi_{0.88}Ge_{0.12}$ alloy at 0 MPa and 360 MPa as illustrated in Figure 2, the relative initial μ is estimated to be approximately 1.32 and 1.84, respectively. Using this data, finite element simulations are conducted to assess the impact of air gap width on the B and ΔB in the piezomagnetic sample and the iron core of the induction coil under the two pressure conditions. As shown in Figure 3D, the B within the piezomagnetic sample increases significantly with air gap width, while the B within the core diminishes rapidly. Based on the changes in B due to the stress change from 0 to 360 MPa, we determine the relationship between the ΔB and the air gap width for the sample and the iron core, as depicted in Figure 3E. The increase in ΔB for the piezomagnetic sample slows down as the air gap spacing increases, potentially due to the saturation tendency of local magnetic poles in the pressure-sensitive branch (Supplementary Figure S2). The ΔB within the core rises initially and peaks at an air gap width of approximately 1.5 mm. Further increasing the air gap leads to a gradual drop in ΔB, which is attributed to the increased magnetic reluctance in the induction coil branch and magnetic flux leakage at the air gap.

The piezomagnetic sample in this study is a composite of $MnCoSi_{0.88}Ge_{0.12}$ alloy particles uniformly mixed with paraffin wax with negligible barocaloric-thermomagnetic effects (Supplementary Figure S1). Here, paraffin wax is employed as a pressure-transmitting medium because of its superior fluidity under pressure. It fills gaps between alloy particles and the pressure vessel, allowing uniform pressure transmission to the particles. In this work, the optimal paraffin mass fraction is experimentally determined to be approximately 10%, effectively balancing pore suppression and preservation of the composite's piezomagnetic performance. Besides, the simulation pressure conditions are 0 and 360 MPa. However, in practical applications, piezomagnetic power generation devices operate under alternating pressures with varying magnitudes. To more accurately and vividly demonstrate the piezomagnetic effect of the $MnCoSi_{0.88}Ge_{0.12}$ composite, we have constructed and tested the prototype device (see Supplementary Information for additional details).

Implementation of piezomagnetic power generation

Utilizing an electronic dynamic pressure testing machine, we subject the prototype device to alternating pressure of varying frequencies and magnitudes. At room temperature conditions (~297.5 K), we apply an alternating pressure with a frequency of 5 Hz and a magnitude ranging from 0 to 100 MPa, as depicted in Figure 4A. Figures 4B-D illustrate the waveforms of the change rate of stress ($\frac{dP}{dt}$), press rod displacement (ΔL) and voltage (V) over time under zero air gap conditions. The observed waveform congruence in both shape and periodicity establishes two critical findings: the piezomagnetic origin of voltage generation in the pressure-sensitive reluctance unit, and the functional validity of the proposed magnetic circuit design. Figures 4E & F demonstrate that as the air gap size increases, the peak values of the induced voltage (V_{peak}) change greatly. When the air gap is optimized to 1.5 mm, the device achieves the highest V output, which is in excellent agreement with the predictions presented in Figure 3E.

To examine the impact of temperature on the performance of the prototype device, we set the air gap to 1.5 mm and explore the relationship

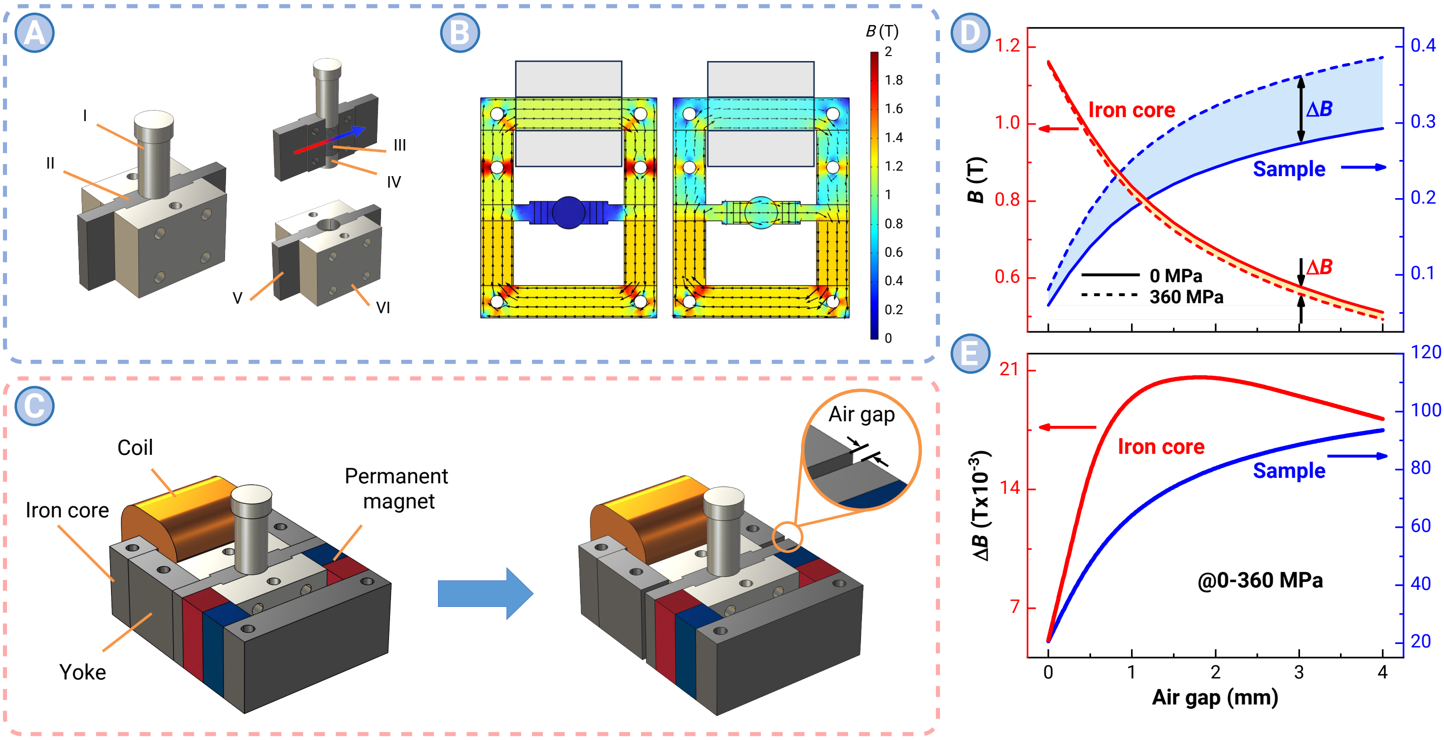

Figure 3. Design of a piezomagnetic power generation device (A) Schematic of a pressure-sensitive magnetic reluctance device based on the piezomagnetic effect. Components are labeled as follows: I, non-magnetic press rod; II, pressure chamber; III, piezomagnetic sample; IV, non-magnetic base; V, magnetic conductive component; VI, non-magnetic component. (B) Comparative illustration of B distribution under two states: left, piezomagnetic sample with lower μ; right, sample with higher μ. (C) Adjustable air gap integrated into the induction coil branch to balance the magnetic reluctance of the two branches. (D) Variation of B in the piezomagnetic sample and induction coil core with air gap width. Solid and dashed lines correspond to pressure conditions of 0 MPa and 360 MPa, respectively. (E) Variation of ΔB with air gap width under the same pressure conditions.

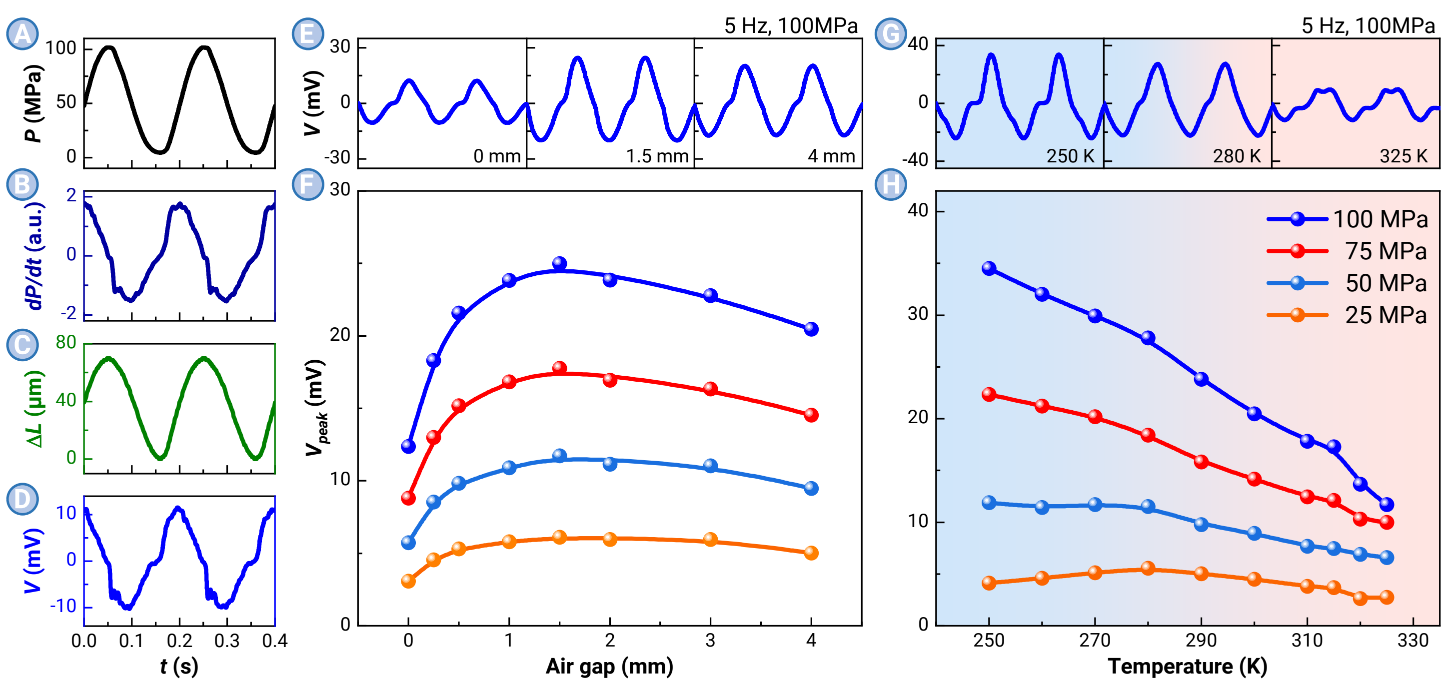

Figure 4. Functional verification of the piezomagnetic power generation device under varying air gaps, temperatures, and driving pressures (A) P-t output generated by the testing machine. (B) Waveform of dP/dt with time. (C) Waveform of ΔL with time. (D) V-t waveform of the prototype device with zero air gap at room temperature. (E) V-t waveform with three different air gap widths at room temperature. (F) Relationship between V_{peak} and air gap width under different pressures at room temperature. (G) V-t waveform with air gaps of 1.5 mm at three different temperatures. (H) Relationship between the V_{peak} and the sample temperature.

between V and the intensity of alternating pressure across a temperature range of 250-325 K. As illustrated in Figures 4G & H, the peak voltage occurs near 280 K in the V_{peak}-T curve when the pressure change is between 0-25 MPa. Expanding the pressure range to 0-50 MPa shifts this peak to lower temperatures, resulting in a more distinct temperature plateau. Further increases in pressure cause the peak temperature to exceed the measured range, indicating that the external pressure can drive a transition from an antiferromagnetic to a ferromagnetic state. It is suggested that higher V_{peak}

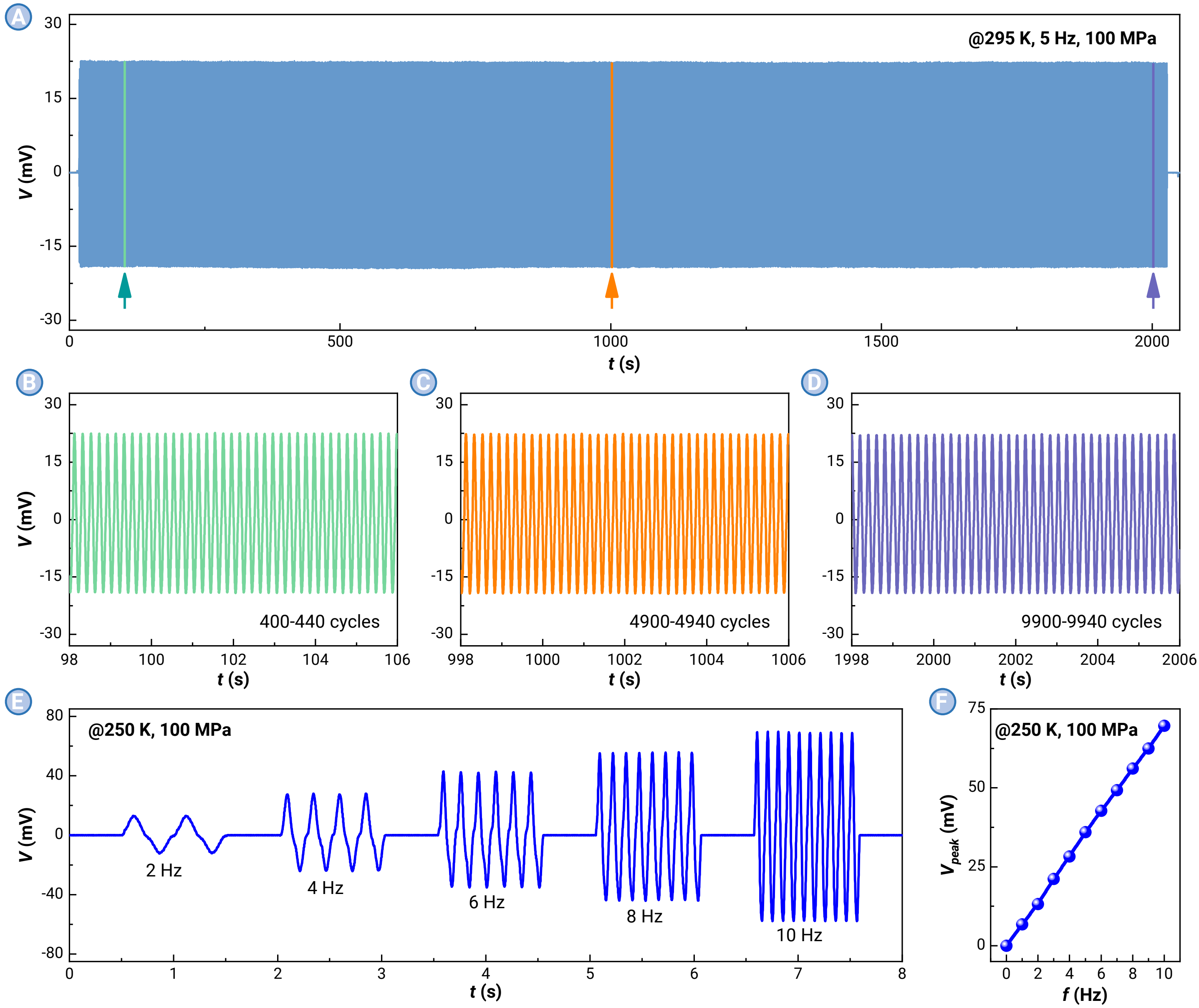

Figure 5. Power generation performance under 100 MPa pressure: time and frequency dependences (A) Complete *V-t* waveform over approximately 10^4 cycles at 295 K and 5 Hz. (B) Segment near the 400th cycle. (C) Segment near the 4900th cycle. (D) Segment near the 9900th cycle. (E) *V-t* waveform for different frequencies at 250 K. (F) Relationship between V_{peak} and driving frequency (the waveforms for odd driving frequencies of 1–9 Hz are omitted for clarity).

output may be achievable with an enlarged driving force. However, considering the limited structural strength of the prototype device, this study does not attempt higher pressures.

To evaluate the repeatability and long-term durability, the prototype device is subject to an alternating pressure of 0-100 MPa at 5 Hz and 295 K for about 10^4 cycles. Figure 5A displays the complete *V-t* waveform, while Figures 5B-D show segments near the 400th, 4900th, and 9900th cycles, respectively. These waveforms exhibit a remarkably stable V_{peak} of approximately 22.5 mV, aligning well with the performance (~22.2 mV) shown in Figure 4H, and demonstrating excellent repeatability and long-term durability. Furthermore, we investigate the relationship between *V* and the frequency of alternating driving pressure, as shown in Figures 5E & F. As the frequency increases from 2 to 10 Hz, the change rate of Φ_m in the induction coil linearly increases, leading to a significant rise in the V_{peak} from approximately 12.9 mV to approximately 69.6 mV. The absence of voltage saturation with increasing frequency reveals an important characteristic of piezomagnetic power generation over thermomagnetic generation—its capacity to operate effectively at higher frequencies. Unlike thermomagnetic generators, which are limited by heat exchange rates between materials and their heat sources or sinks, piezomagnetic devices can capitalize on the rapid transmission of compressive stress in solids (up to several kilometers per second) to achieve higher operational frequencies. This capability enhances the number of working cycles per unit time, thereby boosting power density.

The V_{peak} of 69.6 mV at 250 K and 100 MPa with a frequency of 10 Hz is roughly equivalent to 23.2 mV/g for our piezomagnetic sample. Based on the coil's internal resistance of 150 ohms, the maximum power of the piezomagnetic sample ($\frac{V_{peak}^2}{R}$) is calculated to be 32.3 μW, with a maximum power density of approximately 34.4 μW/cm^3, and an average power density of approximately 12.2 μW/cm^3. Compared to the maximum voltage of 1.92 mV/g, the maximum power density of 1.75 μW/cm^3 and the average power density of 0.5 μW/cm^3 obtained from the experimental optimization of the thermomagnetic power generation material NiMnIn,[29] the values in our study have a clear advantage. Based on the ΔL with applied pressure force (*F*) recorded by the pressure testing machine, the net mechanical energy input power is estimated to be ~0.1 W at 100 MPa and 10 Hz (Supplementary Figure S6). According to the average power of 12.2 μW, the energy conversion efficiency is estimated to be 0.0122 %, significantly lower than conventional piezoelectric (7-27.5%)[45] and thermomagnetic systems (0.1-2%).[29,46] The low efficiency can be primarily attributed to frictional losses between the press rod, the cavity components, and the piezomagnetic composite under high alternating stress. Further studies on the kinematics of the spring-pendulum resonance system and lubrication optimization (e.g., utilizing MoS_2 solid-state lubricant or elastic sealing and bushing structures) of the device are required to enhance the net mechanical energy input power and reduce the frictional losses. Increasing the turns in the induction coil by employing a smaller wire diameter can amplify *V*, thereby facilitating energy storage through a rectifier-capacitor circuit, although this approach may not improve the power density due to the increased coil resistance (see Supplementary Information for additional details).

Finally, to visually demonstrate the output of the alternating *V* due to the piezomagnetic effect, we achieve the periodic flashing of LEDs with the alternating driving pressure, based on the same principle and circuit hardware that has been introduced for the demonstration of thermomagnetic power generation[28,29] (see Supplementary Movie and Supplementary Figure S8 for details).

CONCLUSION

We present a piezomagnetic power generation device that employs the magnetic phase transitions in MnCoSi-based alloys, reliably converting small-displacement mechanical energy into electrical power. Upon addition of Ge into the Si site of MnCoSi, the $MnCoSi_{0.88}Ge_{0.12}$ alloy can exhibit pronounced piezomagnetic properties across a wide temperature range, including room temperature. The magnetic circuit of the piezomagnetic prototype device has been deliberately designed to enhance $\Delta\Phi_m$ within the induction coil. This prototype has been subjected to extensive testing under diverse temperature and pressure conditions, consistently showing compelling performance across a wide temperature span from 250 to 325 K, covering room temperature. Notably, the prototype device, utilizing $MnCoSi_{0.88}Ge_{0.12}$ as the working substance and lacking moving parts, reaches a peak power density of approximately 34.4 μW/cm^3. The piezomagnetic power generation technology offers several advantages. It imposes no strict requirements on the shape and mechanical properties of materials, providing greater flexibility in material selection. Additionally, piezomagnetic materials exhibit longer lifespans and superior impact resistance even at small displacements, which confers advantages in terms of durability and reliability. Furthermore, the device can be separated into two modules connected by a hydraulic tube: a mechanical energy harvesting module and a piezomagnetic generation module, which can further enhance their flexibility and reliability (see Supplementary Figure S9).

Future research could focus on optimizing the piezomagnetic materials and magnetic circuits to enhance energy conversion efficiency. Exploring alternative piezomagnetic materials with superior properties could further improve device performance. Additionally, investigating the kinematics of the spring-pendulum resonance system and optimizing device lubrication are essential for increasing mechanical energy input power and reducing frictional losses. These advancements will collectively strengthen the foundation for sustainable energy solutions in industrial and environmental monitoring. The advantages of piezomagnetic power generation, such as long-term stability and durability in harsh conditions, make it ideal for unattended geological and architectural monitoring applications.

REFERENCES

1. Yang Q., Shen J., Xu R., et al. (2025). Toward sustainable lunar base development: Comprehensive space environment platform. *Innov. Energy* **2**:100076. DOI:10.59717/j.xinn-energy.2025.100076
2. Wang Q., Dan Y., Riffat S., et al. (2024). Harvesting energy from the sun and space: A versatile collector for simultaneous production of electricity, heat, and cold energy. *Innov. Energy* **1**:100013. DOI:10.59717/j.xinn-energy.2024.100013
3. Yin Y., Lin S., Xu Z., et al. (2024). Giant-thermopower ionogels for multifunctional energy harvesting through molecularly selective ionic pairing and hydrogen bonding. *Innov. Energy* **1**:100048. DOI:10.59717/j.xinn-energy.2024.100048
4. Roga S., Bardhan S., Kumar Y., et al. (2022). Recent technology and challenges of wind energy generation: A review. *Sustain. Energy Techn.* **52**:102239. DOI:10.1016/j.seta.2022.102239
5. Champier D. (2017). Thermoelectric generators: A review of applications. *Energy Convers. Manage.* **140**:167–181. DOI:10.1016/j.enconman.2017.02.070
6. Sezer N. and Koç M. (2021). A comprehensive review on the state-of-the-art of piezoelectric energy harvesting. *Nano Energy* **80**:105567. DOI:10.1016/j.nanoen.2020.105567
7. Sharma S., Kiran R., Azad P., et al. (2022). A review of piezoelectric energy harvesting tiles: Available designs and future perspective. *Energy Convers. Manage.* **254**:115272. DOI:10.1016/j.enconman.2022.115272
8. Amer T. S., Bahnasy T. A., Abosheiaha H. F., et al. (2025). The stability analysis of a dynamical system equipped with a piezoelectric energy harvester device near resonance. *J. low freq. noise V. A.* **44**:382–410. DOI:10.1177/14613484241277308
9. Amer T. S., Abdelhfeez S. A., Elbaz R. F., et al. (2025). Investigation of the Dynamical Analysis, Stability, and Bifurcation for a Connected Damped Oscillator with a Piezoelectric Harvester. *J. Vib. Eng. Technol* **13**:155. DOI:10.1007/s42417-024-01641-4
10. Patil D. R., Lee S., Thakre A., et al. (2023). Obtaining a broadband magneto-mechano-electric generator with large power for IoT operation. *J. Mater. Chem. A* **11**:15219–15226. DOI:10.1039/D3TA01587D
11. Patil D. R., Lee S., Thakre A., et al. (2023). Boosting the energy harvesting performance of cantilever structured magneto-mechano-electric generator by controlling magnetic flux intensity on magnet proof mass. *J. Materiomics* **9**:735–744. DOI:10.1016/j.jmat.2023.02.001
12. Park S. H., Kumar A., Kaarthik J., et al. (2020). A Magneto-Mechano-Electric Generator Based on Lead-Free Single-Crystal Fibers for Robust Scavenging of Ambient Magnetic Energy. *Electron. Mater. Lett.* **16**:369–375. DOI:10.1007/s13391-020-00215-2
13. Kumar A., Park S. H., Patil D. R., et al. (2022). Effect of aspect ratio of piezoelectric constituents on the energy harvesting performance of magneto-mechano-electric generators. *Energy* **239**:122078. DOI:10.1016/j.energy.2021.122078
14. Deng Z. and Dapino M. J. (2018). Review of magnetostrictive materials for structural vibration control. *Smart. Mater. Struct* **27**:113001. DOI:10.1088/1361-665x/aadff5
15. Gong J.-H., Zhang Z.-M., Zhang C.-L., et al. (2024). Optimizing magnetoelastic properties by machine learning and high-throughput micromagnetic simulation. *Rare Met.* **43**:2251–2262. DOI:10.1007/s12598-023-02551-2
16. Gong J., Zhang Z., Wang H., et al. (2024). A magnetoelastic effect-guided design for micro stress/strain detector using deep learning. *IEEE Sens. J.* **24**:4350–4355. DOI:10.1109/JSEN.2023.3347853
17. Li X., Yang W., Li C., et al. (2024). Flexible solid-solid phase change material with zero leakage via in-situ preparation for battery thermal management. *Innov. Energy* **1**:100034. DOI:10.59717/j.xinn-energy.2024.100034
18. Kitanovski A. (2020). Energy Applications of Magnetocaloric Materials. *Adv. Energy Mater.* **10**:1903741. DOI:10.1002/aenm.201903741
19. Franco V., Blázquez J. S., Ipus J. J., et al. (2018). Magnetocaloric effect: from materials research to refrigeration devices. *Prog. Mater. Sci.* **93**:112–232. DOI:10.1016/j.pmatsci.2017.10.005
20. Li B., Kawakita Y., Ohira-Kawamura S., et al. (2019). Colossal barocaloric effects in plastic crystals. *Nature* **567**:506–510. DOI:10.1038/s41586-019-1042-5
21. Lloveras P., Aznar A., Barrio M., et al. (2019). Colossal barocaloric effects near room temperature in plastic crystals of neopentylglycol. *Nat. Commun.* **10**:1803. DOI:10.1038/s41467-019-09730-9
22. Zhang C., Wang D., Qian S., et al. (2022). Giant barocaloric effects with a wide refrigeration temperature range in ethylene vinyl acetate copolymers. *Mater. Horiz.* **9**:1293–1298. DOI:10.1039/D1MH01920A
23. Qian S., Geng Y., Wang Y., et al. (2016). A review of elastocaloric cooling: Materials, cycles and system integrations. *Int. J. Refrig.* **64**:1–19. DOI:10.1016/j.ijrefrig.2015.12.001
24. Moya X., Kar-Narayan S. and Mathur N. D. (2014). Caloric materials near ferroic phase transitions. *Nat. Mater.* **13**:439–450. DOI:10.1038/nmat3951
25. Zhang Z., Li K., Lin S., et al. (2023). Thermal batteries based on inverse barocaloric effects. *Sci. Adv.* **9**:eadd0374. DOI:10.1126/sciadv.add0374
26. Ma Z., Chen H., Liu X., et al. (2021). Thermomagnetic generation performance of Gd and La(Fe, Si)$_{13}$H$_y$/In material for low-grade waste heat recovery. *Adv. Sustainable Syst.* **5**:2000234. DOI:10.1002/adsu.202000234
27. Chen H., Ma Z., Liu X., et al. (2022). Evaluation of thermomagnetic generation performance of classic magnetocaloric materials for harvesting low-grade waste heat. *Appl. Energy* **306**:117999. DOI:10.1016/j.apenergy.2021.117999
28. Liu X., Chen H., Huang J., et al. (2023). High-performance thermomagnetic generator controlled by a magnetocaloric switch. *Nat. Commun.* **14**:4811. DOI:10.1038/s41467-023-40634-x
29. Chen H., Liu X., Liu Y., et al. (2024). Excellent thermomagnetic power generation for harvesting waste heat via a second-order ferromagnetic transition. *Mater. Horiz.* **11**:2603–2614. DOI:10.1039/D3MH02225K
30. Seung Choi H., Hur S., Kumar A., et al. (2023). Continuous pyroelectric energy generation with cyclic magnetic phase transition for low-grade thermal energy harvesting. *Appl. Energy* **344**:121271. DOI:10.1016/j.apenergy.2023.121271
31. Chun J., Kishore R. A., Kumar P., et al. (2018). Self-powered temperature-mapping sensors based on thermo-magneto-electric generator. *ACS Appl. Mater. Inter.* **10**:10796–10803. DOI:10.1021/acsami.7b17686
32. Chun J., Song H.-C., Kang M.-G., et al. (2017). Thermo-magneto-electric generator

arrays for active heat recovery system. *Sci. Rep.* **7**:41383. DOI:10.1038/srep41383
33. Barcza A., Gercsi Z., Knight K. S., et al. (2010). Giant magnetoelastic coupling in a metallic helical metamagnet. *Phys. Rev. Lett.* **104**:247202. DOI:10.1103/PhysRevLett.104.247202
34. Hao X., Yang B., Li J., et al. (2023). Achieving a linear magnetostrictive effect in textured MnCoSiGe alloys. *Acta Mater.* **242**:118486. DOI:10.1016/j.actamat.2022.118486
35. Zhao Q.-Z., Tian F.-H., Kong S., et al. (2025). Magnetism-structure triple point morphotropic phase boundary and resulting W-type magnetostrictive effect in $Ni_{50}Mn_{34}Sb_{16-x}Ga_x$ Heusler alloys. *Rare Met.* **44**:1905–1916. DOI:10.1007/s12598-024-03116-7
36. Shi K., Sun Y., Yan J., et al. (2016). Baromagnetic effect in antiperovskite $Mn_3Ga_{0.95}N_{0.94}$ by neutron powder diffraction analysis. *Adv. Mater.* **28**:3761-3767. DOI:10.1002/adma.201600310.
37. Shen F., Zhou H., Hu F., et al. (2021). A distinct spin structure and giant baromagnetic effect in MnNiGe compounds with Fe-doping. *J. Am. Chem. Soc.* **143**:6798–6804. DOI:10.1021/jacs.1c02694
38. Foerster M., Macià F., Statuto N., et al. (2017). Direct imaging of delayed magneto-dynamic modes induced by surface acoustic waves. *Nat. Commun.* **8**:407. DOI:10.1038/s41467-017-00456-0
39. Wang H., Zhang Z., Gong J., et al. (2024). Strain-controlled switching of magnetic skyrmioniums in ultrathin nanodisks. *Appl. Phys. Lett* **125**:162402. DOI:10.1063/5.0231123
40. Liu J., Si Y., Gong Y., et al. (2017). Enhanced magnetic refrigeration performance in metamagnetic MnCoSi alloy by high-pressure annealing. *J. Alloy. Compd.* **701**:858–863. DOI:10.1016/j.jallcom.2017.01.161
41. Liu Y., Xu Z., Qiao K., et al. (2021). Strengthened caloric effect in MnCoSi under combined applications of magnetic field and hydrostatic pressure. *J. Mater. Sci* **56**:20060–20070. DOI:10.1007/s10853-021-06546-1
42. Barcza A., Gercsi Z., Michor H., et al. (2013). Magnetoelastic coupling and competing entropy changes in substituted CoMnSi metamagnets. *Phys. Rev. B* **87**:064410. DOI:10.1103/PhysRevB.87.064410
43. Sandeman K. G., Daou R., Özcan S., et al. (2006). Negative magnetocaloric effect from highly sensitive metamagnetism in $CoMnSi_{1-x}Ge_x$. *Phys. Rev. B* **74**:224436. DOI:10.1103/PhysRevB.74.224436
44. Zavorotnev Y. D., Medvedeva L. I., Todris B. M., et al. (2011). Behavior of antiferromagnetic MnCoSi in a magnetic field under pressure. *J. Magn. Magn. Mater* **323**:2808–2812. DOI:10.1016/j.jmmm.2011.06.019
45. Yang Z., Erturk A. and Zu J. (2017). On the efficiency of piezoelectric energy harvesters. *Extreme Mech. Lett.* **15**:26–37. DOI:10.1016/j.eml.2017.05.002
46. Hur S., Kim S., Kim H.-S., et al. (2023). Low-grade waste heat recovery scenarios: Pyroelectric, thermomagnetic, and thermogalvanic thermal energy harvesting. *Nano Energy* **114**:108596. DOI:10.1016/j.nanoen.2023.108596

FUNDING AND ACKNOWLEDGMENTS

This work is supported by the National Natural Science Foundation of China (NSFC) (Grant Nos. U22A20117 and 52271175). The funders had no role in study design, data collection and analysis, decision to publish, or preparation of the manuscript.

AUTHOR CONTRIBUTIONS

Z. M. Zhang, C. L. Zhang and D. H. Wang conceived the idea and wrote the draft with inputs from T. T. Zhou. The sample growth and high-pressure measurements were performed by Z. M. Zhang, H. C. Wang, X. C. Kan, K. Xu, B. Yang and Z. Li. The piezomagnetic power generation prototype device was designed by C. L. Zhang. The piezomagnetic power generation prototype device and the temperature controlling apparatus were built by T. T. Zhou and C. L. Zhang. The finite element simulation was carried out by T. T. Zhou and Z. H. Chen. The theoretical calculations and analysis were performed by Z. M. Zhang, C. L. Zhang, D. H. Wang, Y. Hu and C. Y. Zhang. Y. L. Li, P. Y. Zhao, P. T. Cheng, and H. H. Fu assisted in validation and visualization. All authors contributed to scientific discussions. The project was supervised by D. H. Wang.

DECLARATION OF INTERESTS

The authors declare no competing interests.

DATA AND MATERIALS AVAILABILITY

Data are available from the corresponding author upon reasonable request.

SUPPLEMENTAL INFORMATION

It can be found online at https://doi.org/10.59717/j.xinn-energy.2025.100098